

Observation of intra-unit-cell superconductivity modulation

Tianheng Wei^{1#}, Yanzhao Liu^{2#}, Wei Ren^{1#}, Ziqiang Wang³ & Jian Wang^{1,4,5*}

¹*International Center for Quantum Materials, School of Physics, Peking University, Beijing 100871, China*

²*Quantum Science Center of Guangdong–Hong Kong–Macao Greater Bay Area (Guangdong), Shenzhen 518045, China*

³*Department of Physics, Boston College, Chestnut Hill, MA 02467, USA*

⁴*Collaborative Innovation Center of Quantum Matter, Beijing 100871, China*

⁵*Hefei National Laboratory, Hefei 230088, China*

[#]These authors contributed equally.

*Corresponding to: jianwangphysics@pku.edu.cn (J.W.)

In unconventional high-temperature (high- T_c) superconductors, the symmetry-breaking electronic orders intertwined with the superconductivity provide important clues for understanding the nature of the unconventional pairing mechanism¹. Recently, an exotic superconducting order showing spatially periodic order parameter modulations and translational symmetry breaking, namely the pair density wave (PDW) state, has attracted broad attention^{2–11}. Without breaking translational symmetry, point group symmetry breaking may also induce superconductivity modulations on different atom sites within a single unit cell. However, the intra-unit-cell superconductivity modulation has never been carefully investigated before. Here, using scanning tunneling microscopy/spectroscopy, we report the observation of intra-unit-cell superconductivity modulations in the superconducting gap size and the coherence peak sharpness in monolayer high- T_c Fe(Te,Se) films epitaxially grown on SrTiO₃(001) substrates. Further analysis shows that the maxima and minima in the superconductivity modulation are centered at the crystallographic locations of the Te/Se atoms, revealing the breaking of the glide-mirror symmetry of the Te/Se atoms in monolayer high- T_c Fe(Te,Se) films grown on SrTiO₃(001). Our findings provide precise microscopic information of superconductivity within the lattice unit cell and indicate that the p -orbital electrons of the Te/Se atoms also play an important role in Cooper pairing in unconventional high- T_c iron-based superconductors.

Superconductivity in quantum materials, irrespective of whether the Cooper pairing on the Fermi surface is mediated by phonons or electronic fluctuations, is described based on the BCS (Bardeen–Cooper–Schrieffer) theory of Cooper pair condensation on the crystal lattice of the superconductors. In a common uniform superconductor, the superconducting properties are invariant going from one unit cell, which generally contains a number of atoms and atomic orbitals, to another unit cell following the lattice translation symmetry. In recent years, a novel form of superconducting state known as the pair density wave (PDW) order has been theoretically proposed^{12–19} and experimentally investigated^{2–11}. A PDW order is formed by Cooper pairs with non-zero center-of-mass momentum \mathbf{Q}_{pdw} , thus breaking the lattice translational symmetry with a spatially modulated superconducting order parameter from unit-cell to unit-cell. The experimental evidence of PDW, albeit coexisting with the uniform superconductivity, has been detected in the high- T_c cuprates^{2–5}, iron-based superconductors^{8,9} and other unconventional superconductors^{7,10,11} with the modulation period spanning several times the lattice constant. Remarkably, uniform superconductivity on the crystal lattice can exhibit intra-unit-cell modulations of superconductivity in principle. Theoretically, this could happen when $\mathbf{Q}_{\text{pdw}} = \mathbf{G}$, i.e., when the Cooper pair center of mass momentum \mathbf{Q}_{pdw} matches the reciprocal lattice vector. Despite being a unique property of lattice superconductors, the intra-unit-cell superconducting modulation has not been carefully investigated before. Given the rather local pairing interactions in short-coherence length unconventional superconductors²⁰, probing and resolving the superconducting modulations inside a unit cell in such superconductors can provide valuable insights on the nature of superconductivity and inner workings of the pairing mechanism.

Here, by using scanning tunneling microscopy/spectroscopy (STM/S), we report the intra-unit-cell superconductivity modulation in a monolayer Fe(Te,Se) film grown on SrTiO₃(001) (STO) substrate, a two-dimensional high- T_c iron-based superconductor. The superconductivity modulation is characterized by both superconducting gap size and coherence peak sharpness modulations with a period of $a_{\text{Te/Se}}$, the distance between neighboring Te/Se atoms in the top or bottom layer that defines the unit cell.

Intra-unit-cell superconductivity variation in 1-UC Fe(Te,Se)/STO

The one-unit-cell (1-UC) thick Fe(Te,Se) films were grown by molecular beam epitaxy (MBE) on STO substrates. Fig. 1a shows the crystal structure of 1-UC Fe(Te,Se) consisting an Fe layer sandwiched between two Te/Se layers. One primary unit cell (marked by orange in Fig. 1a) contains two Fe atoms in the middle layer and two Te/Se atoms in the top and bottom layers. The topmost Te/Se layer exhibits a square lattice structure which is visible in the STM topography. The STM/S measurements were performed at 4.3 K, which is much lower than the superconducting transition temperature (around 60 K) of the Fe(Te,Se) films on STO^{21,22}. Fig. 1b shows the atomically resolved STM topographic image of the 1-UC FeTe_{1-x}Se_x film. The nominal stoichiometry $x \approx 0.7$ is estimated from the thickness of the 2nd layer (around 0.58 nm, Extended data Fig. 1)²³. In Fig. 1c, the sites of Fe and Te/Se atoms in the Fe(Te,Se) film are marked within a unit cell. To gain more electronic information within the unit cell, we compared the tunnelling spectra obtained at the topmost Te/Se sites and the Fe sites. Two typical spectra are plotted in Fig. 1d. Both spectra are U-shaped with two pairs of coherence peaks, indicating the fully gapped superconductivity with two superconducting gap sizes Δ_1 and Δ_2 , which is consistent with

previous reports^{8,21–23}. Strikingly, the two superconducting gap sizes on the Fe site are larger than those on the topmost Te/Se site, suggesting an intra-unit-cell superconducting gap variation in the 1-UC Fe(Te,Se) film.

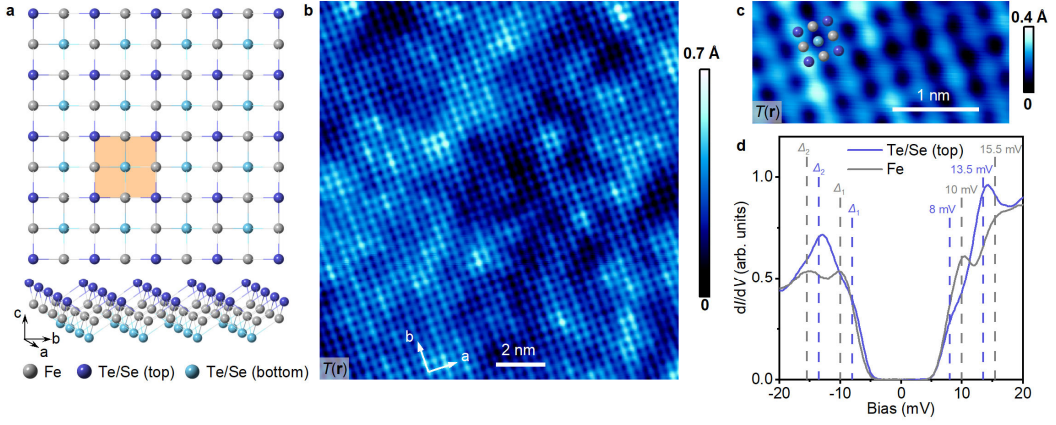


Fig. 1 | STM characterization of the 1-UC Fe(Te,Se) film (Sample 1). **a**, The crystal structure of the 1-UC Fe(Te,Se) film. One primary unit cell is marked by orange, which contains two Fe atoms in the middle layer and two Te/Se atoms in the top and bottom layers. **b**, A atomically resolved topographic image of the 1-UC Fe(Te,Se) film. **c**, A zoom-in of the topographic image of the 1-UC Fe(Te,Se) film. The sites of Fe and Te/Se atoms within one unit cell are marked by colored balls. **d**, Typical tunnelling spectra measured on the topmost Te/Se sites and Fe sites. Both spectra show fully gapped superconductivity and two pairs of coherence peaks. The superconducting gap sizes Δ_1 and Δ_2 on the Fe site ($\Delta_1 \approx 10$ mV, $\Delta_2 \approx 15.5$ mV) are larger than those on the topmost Te/Se site ($\Delta_1 \approx 8$ mV, $\Delta_2 \approx 13.5$ mV), suggesting an intra-unit-cell superconducting gap variation.

Lattice periodic superconductivity modulation

We now focus on the intra-unit-cell superconducting gap variation. High-spatial-resolution tunneling spectra (Fig. 2b) are measured along the topmost Te/Se lattice (red arrow in Fig. 2a). The tunneling spectra show clear two-gap features Δ_1 and Δ_2 marked by two arrows, respectively. As can be seen from the spectra in Fig. 2b, the superconducting coherence peak heights in the spectra show a clear modulation feature along the topmost Te/Se lattice, while the spatial evolution of superconducting gap is relatively difficult to directly distinguish. To determine the superconducting gap size Δ_1 and Δ_2 more precisely, Fig. 2c shows the color map of the $D(V) \equiv -d^3I/dV^3$ calculated from the dI/dV curves shown in Fig. 2b, in which the bias positions of local maxima in $D(V)$ indicate the superconducting gap sizes^{3,8} (Methods). As illustrated in Fig. 2c, both superconducting gap sizes Δ_1 and Δ_2 exhibit the spatial modulation along the top Te/Se lattice. The period of the superconducting gap size modulation is equal to the Te/Se lattice constant $a_{\text{Te/Se}}$, revealing the intra-unit-cell superconducting gap modulation. Figure 2d shows the extracted Δ_1 and Δ_2 values along the distance in Fig. 2c, which directly show the spatial modulation of superconducting gap size along the top Te/Se lattice (red arrow in Fig. 2a). In addition, the robust intra-unit-cell superconducting gap modulations survive and are discernible along a line cut across a vortex in a high magnetic field (Extended data Fig. 3). Moreover, the local D maximum values (purple or blue colors in Fig. 2c) reflect the sharpness of superconducting coherence peaks, which can also serve as a local indicator of superconductivity³. As shown in Fig. 2c and 2d, the

superconducting coherence peak sharpness D_1 or D_2 for superconducting gap Δ_1 or Δ_2 also exhibits spatial modulation with the period of $a_{\text{Te/Se}}$, further confirming the intra-unit-cell modulation of the superconductivity.

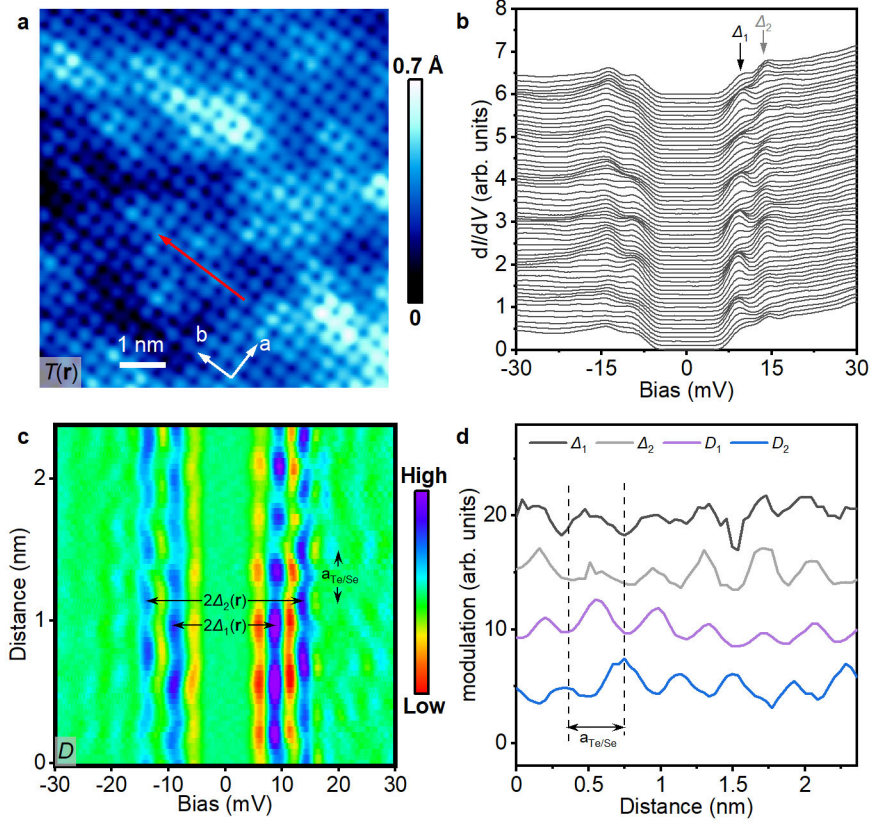


Fig. 2 | Superconductivity modulation with the period of $a_{\text{Te/Se}}$ in 1-UC Fe(Te,Se) film (Sample 1). **a**, A topographic image of the 1-UC Fe(Te,Se) film. **b**, Tunneling spectra measured along the red arrow in **a**. The two arrows indicate the two superconducting gaps Δ_1 and Δ_2 . **c**, Color map of $D \equiv -d^3I/dV^3$ calculated from **b**, which exhibits the spatially modulated superconducting gap sizes (Δ_1 and Δ_2) and coherence peak sharpness (D_1 and D_2). **d**, The extracted superconducting gap sizes (Δ_1 and Δ_2) and coherence peak sharpness (D_1 and D_2) along the distance in **c**. All curves show spatial modulation with the period of the Te/Se lattice constant $a_{\text{Te/Se}}$. The curves are normalized and vertically shifted for comparison. The distances in **c** and **d** are defined relative to the beginning of the arrow in **a**.

Imaging the intra-unit-cell superconductivity modulation

To gain further insights into the intra-unit-cell superconductivity modulation, we carried out spectroscopic imaging STM measurements on a 1-UC Fe(Te,Se) film (Sample 2) prepared with the same recipe as Sample 1. In the region shown in Fig. 3a (Region 1), we extracted superconducting gap sizes Δ_1 and Δ_2 from the tunneling spectrum measured at every pixel (the density of pixels is as high as 625 pixels/nm²) and obtained the superconducting gap maps $\Delta_1(\mathbf{r})$ and $\Delta_2(\mathbf{r})$ (Fig. 3b and 3c). The Fourier transform maps $|\Delta_1(\mathbf{q})|$ and $|\Delta_2(\mathbf{q})|$ (insets of Fig. 3b and 3c) show distinct Fourier peaks at $\mathbf{Q}_{a,b} = (\pm 1, 0)\mathbf{Q}_{\text{Te/Se}}$ and $(0, \pm 1)\mathbf{Q}_{\text{Te/Se}}$, which are the reciprocal lattice vectors, further verifying the intra-unit-cell superconducting gap modulations with the period of $a_{\text{Te/Se}}$. After applying the Fourier filtering (Methods), the intra-unit-cell modulations of Δ_1 and Δ_2

become clearer (Fig. 3d and 3e). In Fig. 3a-e, the black circles mark the topmost Te/Se sites within a single unit cell, to see the superconducting gap modulations across the crystal lattice. The local minima and maxima of the modulation are centered at crystallographic locations of the topmost and bottommost Te/Se atoms, respectively (Fig. 3b-e). The different superconducting gap sizes at the topmost and bottommost Te/Se sites reveal the glide-mirror symmetry breaking effect of the Te/Se atoms in 1-UC Fe(Te,Se)/STO, indicating the important role played by the Te/Se atoms in Cooper pairing. Interestingly, the spatial modulations of the big and small superconducting gaps, $\Delta_1(\mathbf{r})$ and $\Delta_2(\mathbf{r})$, exhibit an in-phase relation and reach the minima at topmost Te/Se sites simultaneously. Moreover, the superconducting gap modulations display an antiphase relation with the atomic topography height of the topmost Te/Se lattice plane.

To further reveal the phase relationship in the whole field of view, we analyzed the relative phase between the superconducting gap (Δ_1 and Δ_2) modulations and atomic topography by using the 2D lock-in method^{4,5,8,24} (see Methods for more details). Figure. 3f shows the distributions of relative phase $\delta\phi_{\mathbf{Q}_i=a,b}^{\Delta_{1,2},T}(\mathbf{r})$ between the phase of superconducting gap modulation $\phi_{\mathbf{Q}_i}^{\Delta_{1,2}}(\mathbf{r})$ and the phase of the atomic topography $\phi_{\mathbf{Q}_i}^T(\mathbf{r})$ in both a and b directions. Both relative phase distributions (black curve for Δ_1 and red curve for Δ_2) peak near $\pm\pi$, showing the in-phase relation between Δ_1 and Δ_2 modulation and the antiphase relation between the superconducting gap modulations and the atomic topography. Moreover, the in-phase relation between the superconducting gap modulation and topography is also detected in another region of Sample 2 (Extended data Fig. 5). Although such an in-phase case is rare in all regions we have measured, it illustrates that the phase of superconducting gap modulation is not strictly locked by the lattice, excluding the possibility that the gap modulation is a pure lattice potential effect.

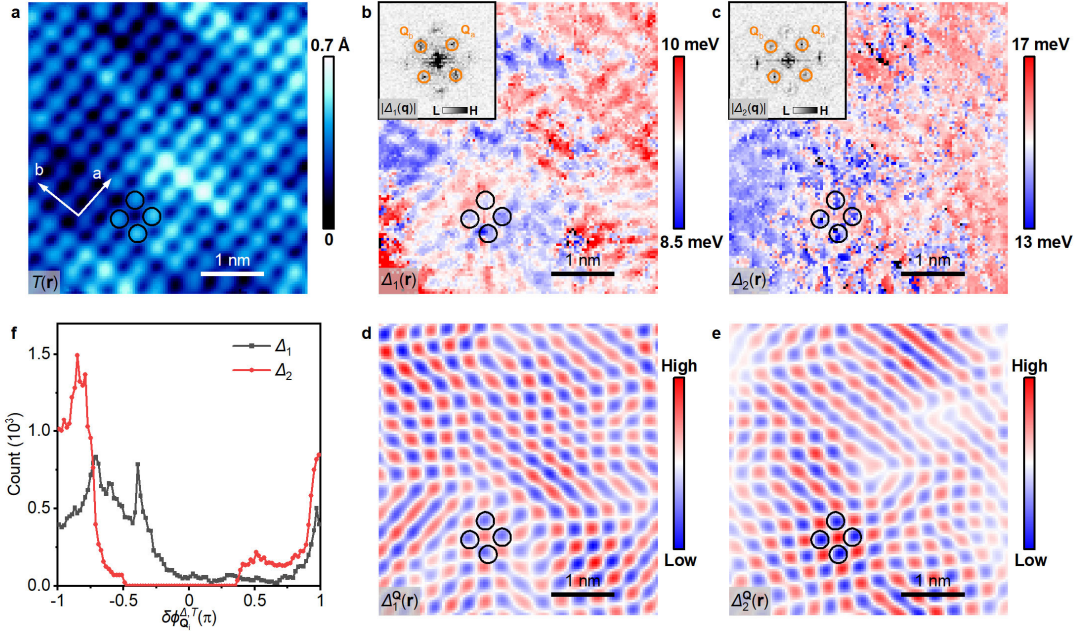


Fig. 3 | Intra-unit-cell superconducting gap modulation in 1-UC Fe(Te,Se) film (Sample 2). **a**, A topographic image of Sample 2 showing the atomic structures of the topmost Te/Se lattice. **b,c**, Superconducting gap maps of Δ_1 (**b**) and Δ_2 (**c**) measured in the same area as in **a**, which show the

intra-unit-cell superconducting gap modulations. The insets of **b** and **c** are the magnitude of the Fourier transform of **b** and **c**, respectively. The modulation wavevector peaks at the Bragg points of the topmost Te/Se lattice (\mathbf{Q}_a and \mathbf{Q}_b) are denoted by orange circles. **d,e**, The Fourier filtered gap map of Δ_1 (**d**) and Δ_2 (**e**). The Fourier filtering process is described in Methods. The topmost Te/Se sites within one unit cell are marked by black circles in **a-e**, clearly revealing the antiphase relation between $\Delta_{1,2}(\mathbf{r})$ and $T(\mathbf{r})$. **f**, The distributions of relative phase between superconducting gap size (Δ_1 in black or Δ_2 in red) and atomic topography. The relative phase distributions peak near $\pm\pi$, approximately showing the antiphase relation between the gap size and the atomic topography.

We know that the superconducting gap size is determined by the energy scale of the pairing interaction, and the coherence peak sharpness is indicative of the strength of superconducting coherence³. Besides the studies on the superconducting gap size, we also extracted and analyzed the coherence peak sharpness maps $D_{1,2}(\mathbf{r})$. As shown in Fig. 4b and 4c, both $D_1(\mathbf{r})$ and $D_2(\mathbf{r})$ maps obtained in Region 1 exhibit clear modulation features. We mark the topmost Te/Se sites by black circles in Fig. 4b and 4c and it is clear that D_1 is locally minimized at top Te/Se sites where D_2 peaks, indicating that the coherence peak sharpness at the large superconducting gap is anticorrelated with that at the small superconducting gap. Such antiphase relation between $D_1(\mathbf{r})$ and $D_2(\mathbf{r})$ is further confirmed by the Fourier filtered D maps (Fig. 4d and 4e) and the distributions of the relative phase $\delta\phi_{\mathbf{Q}_{i=a,b}}^{D_{1,2},T}(\mathbf{r})$ between the phase of coherence peak sharpness modulations

$\phi_{\mathbf{Q}_i}^{D_{1,2}}(\mathbf{r})$ and the phase of the atomic topography $\phi_{\mathbf{Q}_i}^T(\mathbf{r})$ (Fig. 4f) in both a and b directions. The antiphase relation between $D_1(\mathbf{r})$ and $D_2(\mathbf{r})$ is repeatable in all regions measured in all samples (two typical results are shown in Extended data Figs. 6 and 8). The intra-unit-cell modulation of the coherence peak sharpness reflects the superconducting coherence variance within a single unit cell, which provides further evidence of the intra-unit-cell superconductivity modulation in the monolayer Fe(Te,Se)/STO films.

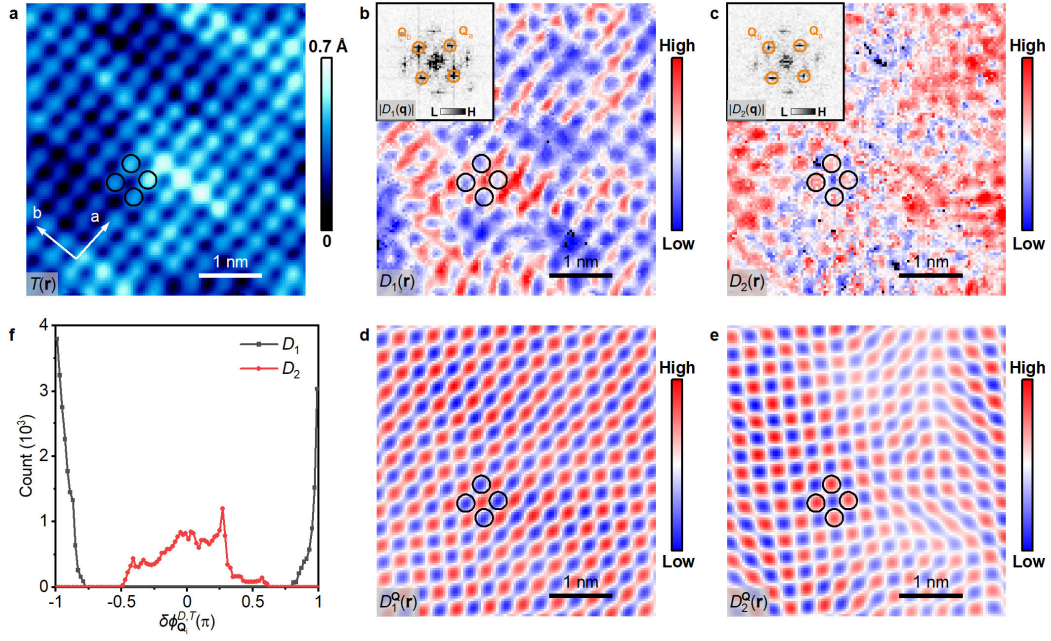


Fig. 4 | Intra-unit-cell superconducting coherence peak sharpness modulation in 1-UC Fe(Te,Se) film (Sample 2). **a**, Topographic image in Fig. 3a. **b,c**, Superconducting coherence peak sharpness maps of D_1 (**b**) and D_2 (**c**) measured in the same area as in **a**, which show the intra-unit-cell D modulation. The insets of **b** and **c** are the magnitude of the Fourier transform of **b** and **c**, respectively. The modulation wavevector peaks at the Bragg points of the topmost Te/Se lattice (Q_a and Q_b) are denoted by orange circles. **d,e**, The Fourier filtered D map of D_1 (**d**) and D_2 (**e**). The Fourier filter process only keeps the Fourier peaks around Q_a and Q_b (Methods). The topmost Te/Se sites within one unit cell are marked by black circles in **a-e**. **f**, The distributions of relative phase between superconducting coherence peak sharpness (D_1 in black or D_2 in red) and atomic topography. The relative phase distributions peak near $\pm\pi$ (0) for D_1 (D_2), approximately showing antiphase (in-phase) relation between the D_1 (D_2) and the atomic topography.

Discussion

Comparing with the previously reported PDW states with period spanning multiple unit cells, the superconductivity modulations in the 1-UC Fe(Te,Se) films have the same period as the unit cell of the crystal lattice containing two Fe atoms and two Te/Se atoms. Therefore, the observed superconductivity modulations carry the reciprocal lattice wavevector and do not break the lattice translational symmetry, which is fundamentally different from the PDW order. Specifically, both the superconducting gap size and the coherence peak sharpness show significant differences between the topmost and bottommost Te/Se atom sites within one unit cell. For a freestanding monolayer film, the two kinds of Te/Se atom sites should be equivalent under glide-mirror reflection operation. However, in our monolayer films, the glide-mirror symmetry breaking is naturally introduced by the STO substrate, which is believed to be vital for the dramatically enhanced high superconducting transition temperature of the monolayer Fe(Te,Se)/STO film family^{25–27}.

Surprisingly, despite the intriguing modulation of the superconductivity detected between the top

and bottom Te/Se locations in the unit cell, we observe no significant differences in the superconducting properties at the two Fe atoms in the unit cell. These findings provide microscopic evidence for the importance of the Te/Se atoms in the superconducting pairing interactions. This is supported by the theoretical proposal that the p -orbitals of the pnictogen and chalcogen can play a significant part in the pairing interactions mediated by electronic spin as well as charge and orbital fluctuations, in addition to the Fe d -orbital electrons of the Fe in iron-based superconductors^{28,29}. The strong p - d hybridization can enhance the effective antiferromagnetic coupling between the d -electrons of the next nearest neighboring Fe atoms, which is known to mediate s_{\pm} pairing in iron-based superconductors³⁰⁻³⁴. The imbalance between the top and bottom Te/Se atoms, induced by the STO substrate, may lead to different pairing strengths and thus the observed intra-unit cell superconductivity modulation. In addition, in most cases, larger superconducting gaps Δ_1 and Δ_2 are observed at the bottom Te/Se sites in contact with the STO substrate, compared to the smaller values at the top Te/Se sites (Fig. 3). This indicates a stronger pairing strength at the bottom Te/Se layer, possibly due to assisted pairing from the phonons in the STO substrate²⁷. As shown schematically in Fig. 5, the next nearest neighbor pairing mediated by the top (bottom) Te/Se is represented by pairing bonds of different strength marked by yellow (orange), forming a staggered Fe-cornered checkboard lattice. Each Fe atom is connected with two strong pairing bonds and two weak pairing bonds, which prevent the Fe site to be at the modulation extremes of superconductivity. In contrast, the Te/Se atoms are centered at either two strong pairing bonds or two weak pairing bonds, leading to the superconductivity difference between the top and bottom Te/Se sites. Our observations are overall consistent with this theoretical scenario.

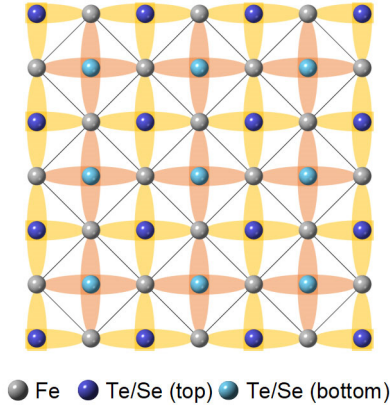


Fig. 5 | Possible theoretical scenario for the intra-unit-cell gap modulation. Schematic for the Te/Se assistant Cooper pairing between next nearest neighbor Fe atoms. Due to the STO substrate induced glide-mirror symmetry breaking, the top and bottom Te/Se are different, leading to different antiferromagnetic coupling strengths and pairing strengths (marked by yellow and orange crosses).

To conclude, we reported the discovery of intra-unit-cell superconductivity modulations in monolayer Fe(Te,Se)/STO, which may be attributed to the glide-mirror symmetry breaking induced by the STO substrate. The modulation peaks and valleys are centered at the Te/Se atom sites and imply the essential role of the Te/Se atom in providing the pairing interaction. Our

findings provide the precise microscopic visualization of local superconductivity within the lattice unit cell and offer new insights into the pairing mechanism of unconventional superconductors containing multiple atoms per unit cell.

References

1. Fradkin, E., Kivelson, S. A. & Tranquada, J. M. Colloquium: Theory of intertwined orders in high temperature superconductors. *Rev. Mod. Phys.* **87**, 457–482 (2015).
2. Hamidian, M. H. *et al.* Detection of a Cooper-pair density wave in $\text{Bi}_2\text{Sr}_2\text{CaCu}_2\text{O}_{8+x}$. *Nature* **532**, 343–347 (2016).
3. Ruan, W. *et al.* Visualization of the periodic modulation of Cooper pairing in a cuprate superconductor. *Nat. Phys.* **14**, 1178–1182 (2018).
4. Edkins, S. D. *et al.* Magnetic field-induced pair density wave state in the cuprate vortex halo. *Science* **364**, 976–980 (2019).
5. Du, Z. *et al.* Imaging the energy gap modulations of the cuprate pair-density-wave state. *Nature* **580**, 65–70 (2020).
6. Liu, X., Chong, Y. X., Sharma, R. & Davis, J. C. S. Discovery of a Cooper-pair density wave state in a transition-metal dichalcogenide. *Science* **372**, 1447–1452 (2021).
7. Chen, H. *et al.* Roton pair density wave in a strong-coupling kagome superconductor. *Nature* **599**, 222–228 (2021).
8. Liu, Y. *et al.* Pair density wave state in a monolayer high- T_c iron-based superconductor. *Nature* **618**, 934–939 (2023).
9. Zhao, H. *et al.* Smectic pair-density-wave order in $\text{EuRbFe}_4\text{As}_4$. *Nature* **618**, 940–945 (2023).
10. Aishwarya, A. *et al.* Magnetic-field-sensitive charge density waves in the superconductor UTe_2 . *Nature* **618**, 928–933 (2023).
11. Gu, Q. *et al.* Detection of a pair density wave state in UTe_2 . *Nature* **618**, 921–927 (2023).
12. Himeda, A., Kato, T. & Ogata, M. Stripe States with Spatially Oscillating d -Wave Superconductivity in the Two-Dimensional t - t' - J Model. *Phys. Rev. Lett.* **88**, 117001 (2002).
13. Chen, H.-D., Vafek, O., Yazdani, A. & Zhang, S.-C. Pair Density Wave in the Pseudogap State of High Temperature Superconductors. *Phys. Rev. Lett.* **93**, 187002 (2004).
14. Berg, E. *et al.* Dynamical Layer Decoupling in a Stripe-Ordered High- T_c Superconductor. *Phys. Rev. Lett.* **99**, 127003 (2007).
15. Agterberg, D. F. & Tsunetsugu, H. Dislocations and vortices in pair-density-wave superconductors. *Nat. Phys.* **4**, 639–642 (2008).
16. Berg, E., Fradkin, E. & Kivelson, S. A. Theory of the striped superconductor. *Phys. Rev. B* **79**, 064515 (2009).
17. Berg, E., Fradkin, E. & Kivelson, S. A. Charge-4e superconductivity from pair-density-wave order in certain high-temperature superconductors. *Nat. Phys.* **5**, 830–833 (2009).
18. Lee, P. A. Amperian Pairing and the Pseudogap Phase of Cuprate Superconductors. *Phys. Rev. X* **4**, 031017 (2014).
19. Agterberg, D. F. *et al.* The Physics of Pair-Density Waves: Cuprate Superconductors and Beyond. *Annu. Rev. Condens. Matter Phys.* **11**, 231–270 (2020).
20. Blatter, G., Feigel'man, M. V., Geshkenbein, V. B., Larkin, A. I. & Vinokur, V. M. Vortices in high-temperature superconductors. *Rev. Mod. Phys.* **66**, 1125–1388 (1994).
21. Chen, C., Liu, C., Liu, Y. & Wang, J. Bosonic Mode and Impurity-Scattering in Monolayer $\text{Fe}(\text{Te},\text{Se})$ High-Temperature Superconductors. *Nano Lett.* **20**, 2056–2061 (2020).
22. Chen, C. *et al.* Atomic line defects and zero-energy end states in monolayer $\text{Fe}(\text{Te},\text{Se})$

- high-temperature superconductors. *Nat. Phys.* **16**, 536–540 (2020).
23. Li, F. *et al.* Interface-enhanced high-temperature superconductivity in single-unit-cell FeTe_{1-x}Se_x films on SrTiO₃. *Phys. Rev. B* **91**, 220503 (2015).
 24. Fujita, K. *et al.* Direct phase-sensitive identification of a *d*-form factor density wave in underdoped cuprates. *Proc. Natl. Acad. Sci.* **111**, E3026–E3032 (2014).
 25. Wang, Q.-Y. *et al.* Interface-Induced High-Temperature Superconductivity in Single Unit-Cell FeSe Films on SrTiO₃. *Chin. Phys. Lett.* **29**, 037402 (2012).
 26. Zhang, W.-H. *et al.* Direct Observation of High-Temperature Superconductivity in One-Unit-Cell FeSe Films. *Chin. Phys. Lett.* **31**, 017401 (2014).
 27. Lee, J. J. *et al.* Interfacial mode coupling as the origin of the enhancement of T_c in FeSe films on SrTiO₃. *Nature* **515**, 245–248 (2014).
 28. Zhou, S., Kotliar, G. & Wang, Z. Extended Hubbard model of superconductivity driven by charge fluctuations in iron pnictides. *Phys. Rev. B* **84**, 140505 (2011).
 29. Yanagi, Y., Yamakawa, Y. & Ōno, Y. Two types of *s*-wave pairing due to magnetic and orbital fluctuations in the two-dimensional 16-band *d-p* model for iron-based superconductors. *Phys. Rev. B* **81**, 054518 (2010).
 30. Mazin, I. I., Singh, D. J., Johannes, M. D. & Du, M. H. Unconventional Superconductivity with a Sign Reversal in the Order Parameter of LaFeAsO_{1-x}F_x. *Phys. Rev. Lett.* **101**, 057003 (2008).
 31. Kuroki, K. *et al.* Unconventional Pairing Originating from the Disconnected Fermi Surfaces of Superconducting LaFeAsO_{1-x}F_x. *Phys. Rev. Lett.* **101**, 087004 (2008).
 32. Chubukov, A. V., Efremov, D. V. & Eremin, I. Magnetism, superconductivity, and pairing symmetry in iron-based superconductors. *Phys. Rev. B* **78**, 134512 (2008).
 33. Hirschfeld, P. J., Korshunov, M. M. & Mazin, I. I. Gap symmetry and structure of Fe-based superconductors. *Rep. Prog. Phys.* **74**, 124508 (2011).
 34. Fernandes, R. M. *et al.* Iron pnictides and chalcogenides: a new paradigm for superconductivity. *Nature* **601**, 35–44 (2022).

Methods

Sample growth and STM measurement

Our experiments were performed on a commercial USM-1600 ultra-high vacuum MBE-STM combined system. The Nb-doped SrTiO₃(001) (wt 0.7%) substrates were annealed at 1000°C in MBE chamber for 1 hour and then cooled down to 330°C for film growth. High purity Fe(99.995%), Te(99.9999%) and Se(99.999%) were codeposited on substrates from Knudsen cells for 9 minutes. Then the as-grown films were annealed at 400°C for 17 hours and transported to the *in situ* low temperature STM kept at 4.3 K. All STM/S measurements were performed at 4.3 K with polycrystalline PtIr tips. The STS spectra were acquired by standard lock-in technique with $V_{\text{mod}} = 0.8$ mV at 983 Hz. The setpoint for all results was $V_s = 40$ mV, $I_s = 500$ pA unless stated otherwise.

Extraction of superconducting gap size and coherence peak sharpness

Due to the intra-unit-cell modulations of superconductivity, the coherence peak structures of superconductivity could degrade into shoulder structures as shown in Extended data Fig. 2. To clearly reveal the peak and shoulder structures with the same method, we took the negative second derivative of the dI/dV spectra, namely the D spectra ($D \equiv -d^2I/dV^2$), to characterize the coherence peak structure. The peaks in D spectra correspond to the superconducting gap shown as peak or shoulder structures in dI/dV spectra. The larger peak value of D represents sharper coherence peak. Thus, we extracted superconducting gap size and coherence peak sharpness as follows:

1. Calculate the D spectra from the dI/dV spectra;
2. Find the bias V_1^0 and V_2^0 that have local maxima values of D near the two superconducting gap energy Δ_1 and Δ_2 extracted from the spatial averaged STS, respectively.
3. For each bias V_i^0 ($i = 1,2$), use three data points of $D(V)$ in the neighborhood of V_i^0 , namely $\{V_i^{-1}, V_i^0, V_i^{+1}\}$, to fit a quadratic function and take the apex position eV_i as the gap value Δ_i , and the apex value as the coherence peak sharpness D_i .

For both positive (+) and negative (-) bias we can extract $\Delta_{i=1,2}^{+(-)}$ and $D_{i=1,2}^{+(-)}$. The Δ and D shown in figures are $\Delta_{i=1,2} = (\Delta_{i=1,2}^+ + \Delta_{i=1,2}^-)/2$ and $D_{i=1,2} = (D_{i=1,2}^+ + D_{i=1,2}^-)/2$. For rare cases that gap extraction processes failed, the corresponding pixels were labeled as “bad pixels” and plotted in black in the $\Delta(\mathbf{r})$ and $D(\mathbf{r})$ maps. Extended data Fig. 2 shows a typical example of the gap extraction results.

Relative phase analysis based on 2D lock-in method

To quantitatively determine which atomic sites are the modulation extremes centered at, we need to compare the phase information of topography and modulation maps. However, typical Fourier map only shows the intensity of Fourier transform and the detailed phase information is absent. To extract the detailed phase information of modulations with wavevector \mathbf{Q} in real space map $C(\mathbf{r})$, we used 2D lock-in method to calculate the spatial complex amplitudes of the modulations as follows:

$$A_{\mathbf{Q}}^C(\mathbf{r}) = F^{-1} \left[F[C(\mathbf{r})e^{i\mathbf{Q}\cdot\mathbf{r}}] \cdot \frac{1}{2\pi\sigma_q^2} e^{-\frac{\mathbf{q}^2}{2\sigma_q^2}} \right]$$

where F and F^{-1} are Fourier transform and inverse Fourier transform, \mathbf{q} is the coordinate in Fourier space and σ_q is the cut-off length in Fourier space. In practice, we chose $\sigma_q = 1/\lambda$ and λ is the period of the modulation ($\lambda = 2\pi/Q$). From the spatial complex amplitude, we can extract its phase as a phase map:

$$\phi_{\mathbf{Q}}^C(\mathbf{r}) = \text{Arg}\left(A_{\mathbf{Q}}^C(\mathbf{r})\right)$$

We obtained phase maps at $\mathbf{Q}_{a,b}$ for atomic topography $T(\mathbf{r})$, superconducting gap map $\Delta_{1,2}(\mathbf{r})$ and superconducting coherence peak sharpness map $D_{1,2}(\mathbf{r})$, respectively. The relative phase $\delta\phi_{\mathbf{Q}_{a,b}}^{\Delta/D,T}(\mathbf{r})$ between $\phi_{\mathbf{Q}_{a,b}}^{\Delta/D}(\mathbf{r})$ and $\phi_{\mathbf{Q}_{a,b}}^T(\mathbf{r})$ reflect the relative shift between superconductivity modulations and atomic topography. Extended data Fig. 4 shows a typical example of the relative phase between $\phi_{\mathbf{Q}_{a,b}}^{D_1}(\mathbf{r})$ and $\phi_{\mathbf{Q}_{a,b}}^T(\mathbf{r})$. The statistical distributions of relative phases $\delta\phi_{\mathbf{Q}_{a,b}}^{D_1,T}(\mathbf{r})$ in both a and b directions peak around $\pm\pi$, showing antiphase relation between D_1 and the atomic topography height of the topmost Te/Se lattice plane.

Fourier filtering process

The Fourier filtering was performed by multiplying Gaussian windows centered at Fourier peaks \mathbf{Q}_i in Fourier map. Then take inverse Fourier transform of the masked Fourier map to get the filtered map. The process is realized as below:

$$C^{\mathbf{Q}}(\mathbf{r}) = F^{-1}\left[F[C(\mathbf{r})] \cdot \sum_i \frac{1}{2\pi\sigma_q^2} e^{-\frac{(\mathbf{q}-\mathbf{Q}_i)^2}{2\sigma_q^2}}\right]$$

where $C(\mathbf{r})$ is the real space map. In practice, \mathbf{Q}_i are Bragg peaks of top Te/Se lattice and σ_q is $1/a_{\text{Te/Se}}$.

Data Availability

All data that support the findings of this study are available from the corresponding author on reasonable request.

Code Availability

The code used to analyze the data reported in this study is available from the corresponding authors on reasonable request.

Acknowledgements

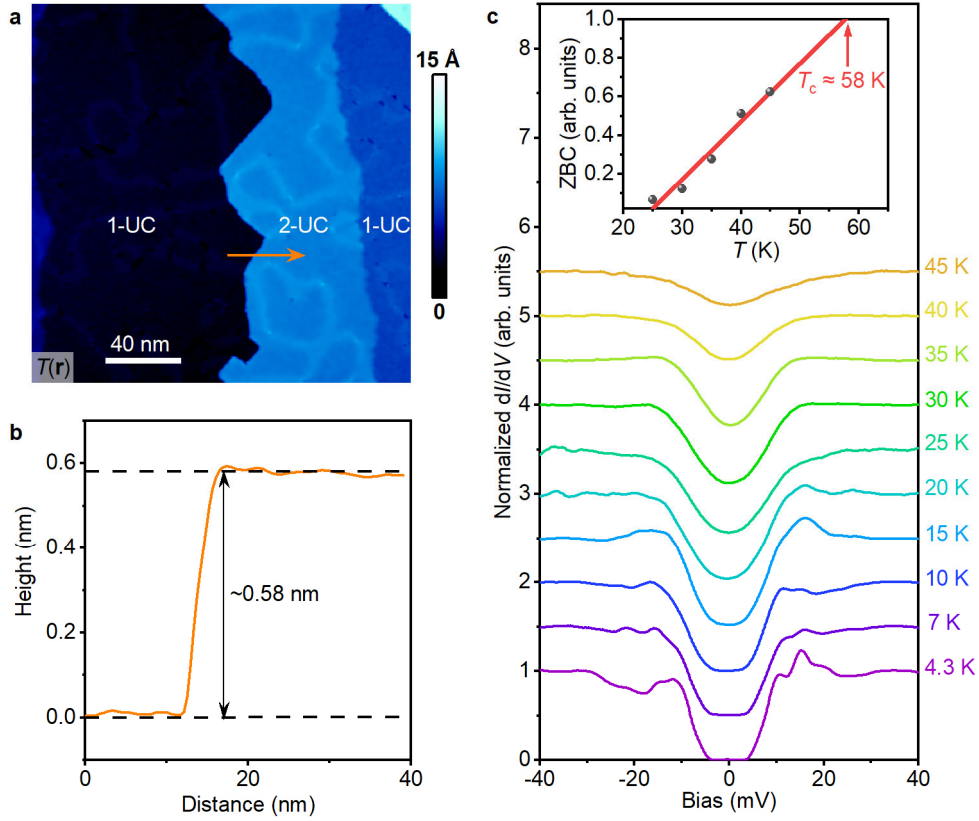
We thank Patrick A. Lee, Michał Papaj and Lingyuan Kong for discussions and Zhen Liang for help with data analyses. This work was supported by the National Natural Science Foundation of China (Grant No. 12488201), the Innovation Program for Quantum Science and Technology (2021ZD0302403). Z.W. is supported by the U.S. Department of Energy, Basic Energy Sciences Grant No. DE-FG02-99ER45747.

Author contributions

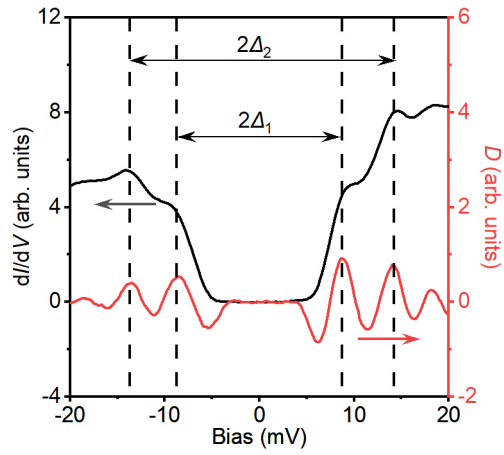
J.W. conceived and supervised the research. T.W., W.R. and Y.L. grew the samples and carried out the STM/STS experiments. T.W., Y.L., W.R. and J.W. analyzed the experimental data. T.W., Y.L., Z.W. and J.W. wrote the manuscript.

Competing interests

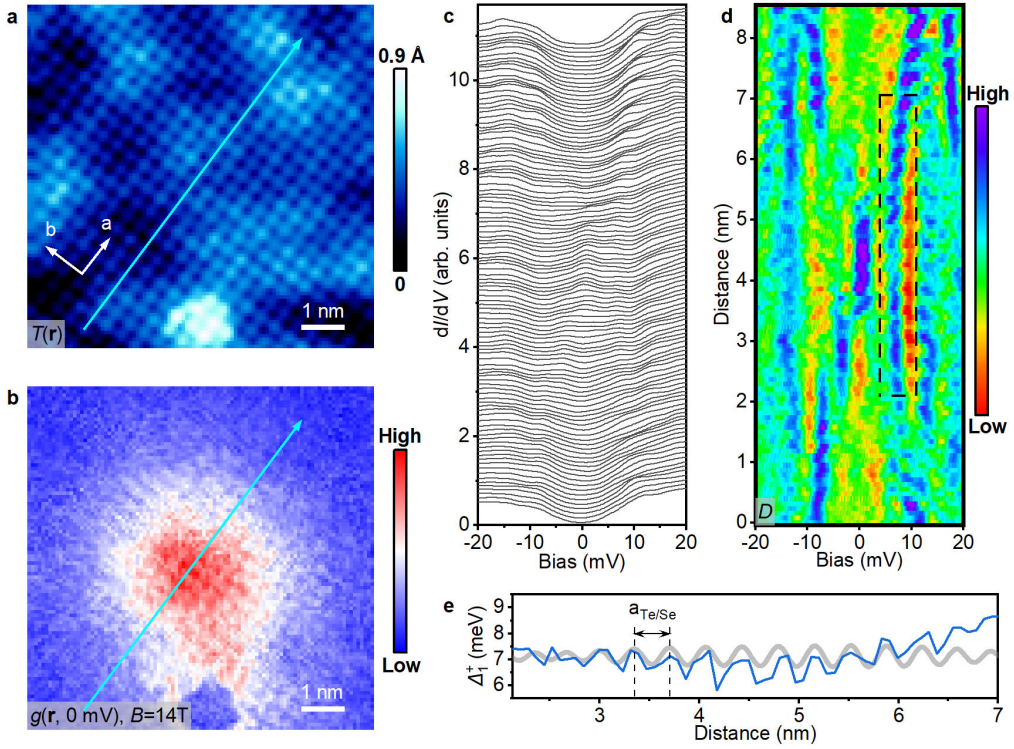
The authors declare no competing interests.



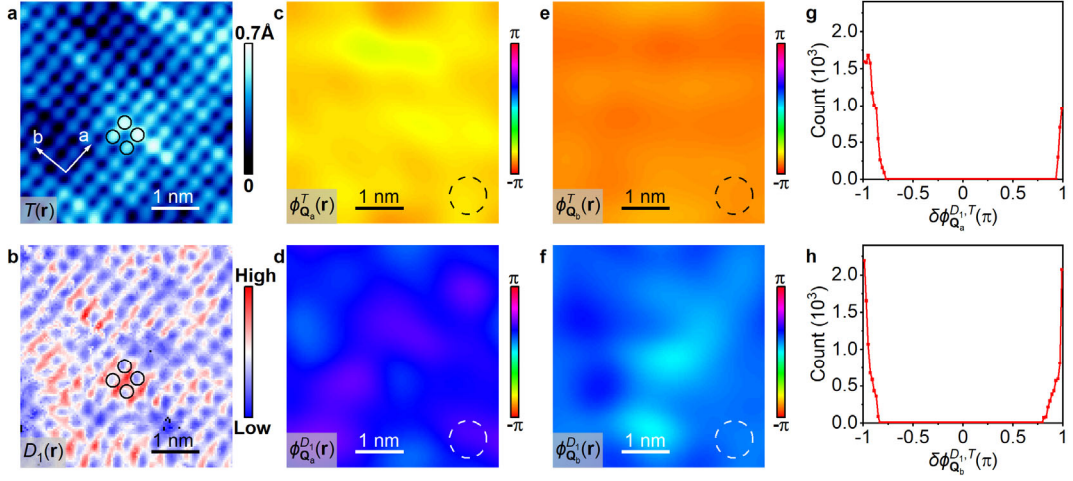
Extended data Fig. 1 | More information about the 1-UC Fe(Te,Se)/STO (Sample 2). **a**, A large scale topographic image of the Fe(Te,Se)/STO film with terrace of STO substrate and partially grown 2nd-UC Fe(Te,Se). $V_s = 1$ V, $I_s = 100$ pA. **b**, The altitude line profile taken along orange arrow in **a**. The thickness of 2nd-UC FeTe_{1-x}Se_x is around 0.58 nm, corresponding to $x \approx 0.7$. **c**, The temperature dependence of the normalized tunnelling spectra, which are obtained by dividing the cubic fitting to the spectra for $|V| \geq 30$ mV. The inset image shows the zero-bias conductance (ZBC) extracted from the normalized tunnelling spectra, yielding an extrapolated gap closing T_c of 58 K when the zero-bias conductance is 1.



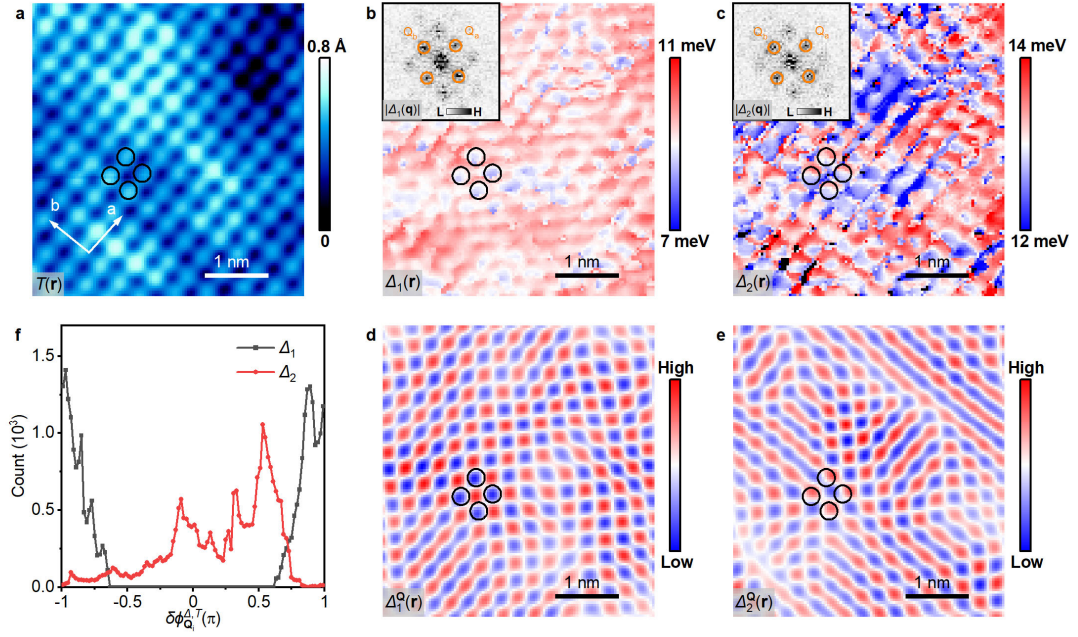
Extended data Fig. 2 | Extraction of superconducting gap. Black curve shows a typical dI/dV spectrum with two pairs of superconducting coherence peaks. Red curve shows the $D \equiv -d^3I/dV^3$ spectrum, which shows clear peak features at the superconducting gap energy marked by black dashed lines.



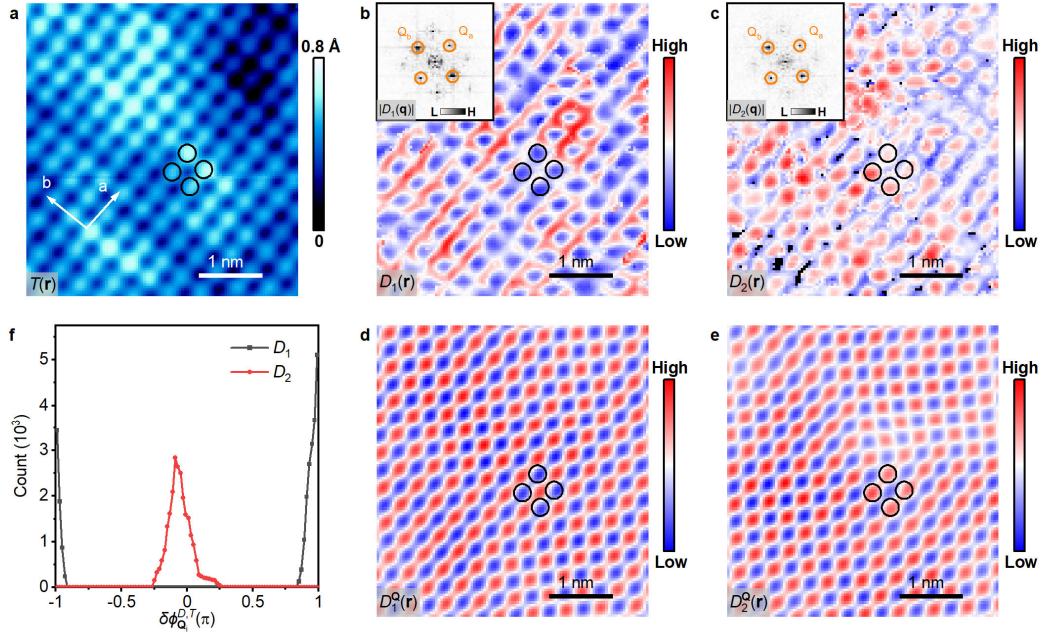
Extended data Fig. 3 | Robust intra-unit-cell superconducting gap modulation across a vortex in high magnetic field (Sample 1). **a**, A topographic image of Sample 1. **b**, Zero bias conductance map $g(\mathbf{r}, 0 \text{ mV}) \equiv dI/dV(\mathbf{r}, V = 0 \text{ mV})$ measured in the same area of **a** under a c -axis magnetic field of $B = 14 \text{ T}$. A single vortex is clearly revealed by higher zero bias conductance. **c**, Tunneling spectra measured along the cyan arrow in **a** and **b** at $B = 14 \text{ T}$. The cut line is chosen by the top Te/Se lattice direction across the vortex. Both the gap edges and the bound states in the vortex core are visible. **d**, Color map of $D \equiv -d^3I/dV^3$ calculated from **c**, which exhibits the spatially modulated superconducting gap size. **e**, The extracted superconducting gap size at positive bias (Δ_1^+) within the dashed rectangle in **d**. The gap sizes Δ_1^+ exhibit spatial modulation along the top Te/Se lattice with a period of $a_{\text{Te/Se}}$. The gray curve is the extracted gap size modulation by applying Fourier filter.



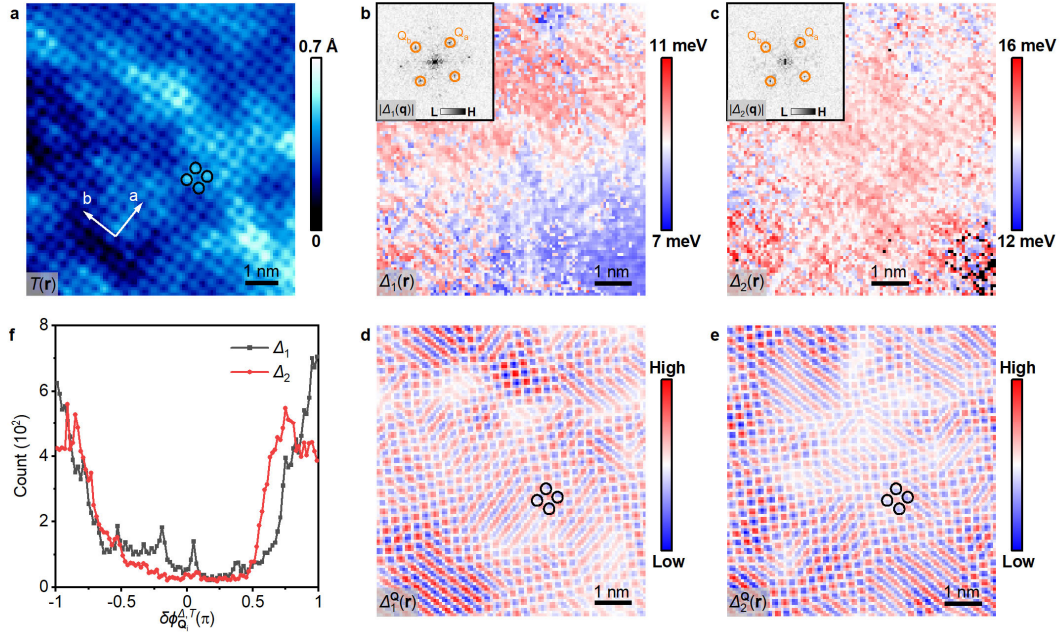
Extended data Fig. 4 | Relative phase extraction. **a,b**, The topographic image $T(\mathbf{r})$ and the coherence peak sharpness map $D_1(\mathbf{r})$ of Region 1 shown in Fig. 4. The topmost Te/Se sites within one unit cell are marked by black circles in **a** and **b**, indicating the antiphase relation between $D_1(\mathbf{r})$ and $T(\mathbf{r})$. **c,d**, Phase maps of $T(\mathbf{r})$ and $D_1(\mathbf{r})$ of modulation at \mathbf{Q}_a . **e,f**, Phase maps of $T(\mathbf{r})$ and $D_1(\mathbf{r})$ of modulation at \mathbf{Q}_b . **g,h**, Distributions of relative phase $\delta\phi_{\mathbf{Q}_i}^{D_1, T}(\mathbf{r})$ between $\phi_{\mathbf{Q}_i}^{D_1}(\mathbf{r})$ and $\phi_{\mathbf{Q}_i}^T(\mathbf{r})$, further suggesting the overall antiphase relation ($\delta\phi \approx \pm\pi$) between $T(\mathbf{r})$ and $D_1(\mathbf{r})$.



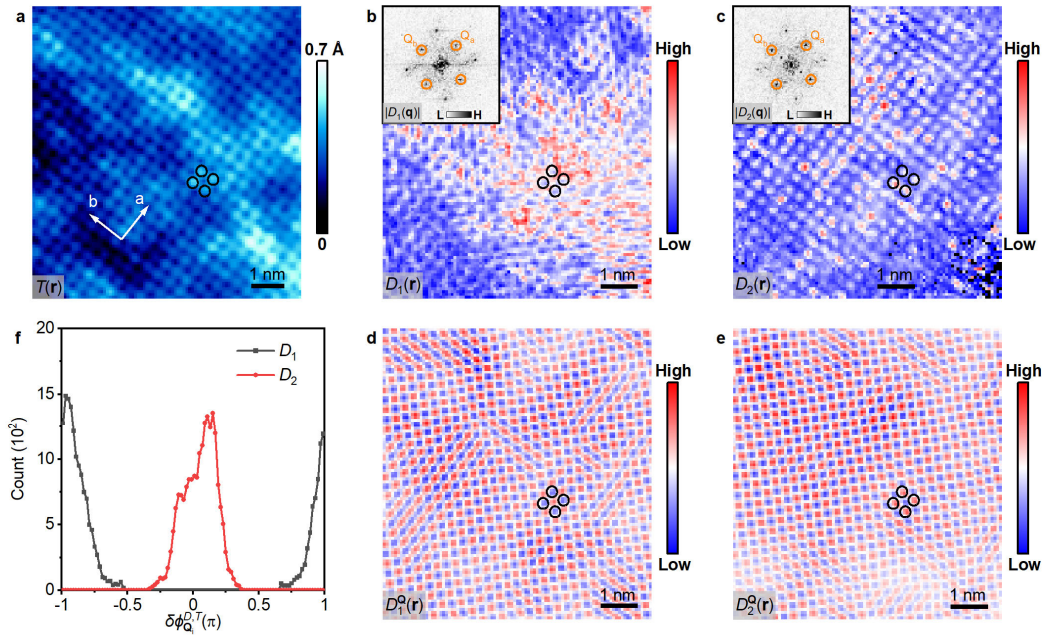
Extended data Fig. 5 | Intra-unit-cell superconducting gap modulation in another region (Region 2) of Sample 2. **a**, The topographic image of Region 2. **b,c**, Superconducting gap maps of Δ_1 (**b**) and Δ_2 (**c**) measured in the same area as in **a**, which show the intra-unit-cell superconducting gap modulations. The insets of **b** and **c** are the magnitude of the Fourier transform of **b** and **c**, respectively. The modulation wavevector peaks at the Bragg points of the topmost Te/Se lattice (\mathbf{Q}_a and \mathbf{Q}_b) are denoted by orange circles. **d,e**, The Fourier filtered gap map of Δ_1 (**d**) and Δ_2 (**e**). The topmost Te/Se sites within one unit cell are marked by black circles in **a-e**, revealing the antiphase relation between $\Delta_1(\mathbf{r})$ and $T(\mathbf{r})$ and nearly in-phase relation between $\Delta_2(\mathbf{r})$ and $T(\mathbf{r})$. **f**, The distributions of relative phase between superconducting gap size (Δ_1 in black or Δ_2 in red) and atomic topography. The relative phase distributions peak near $\pm\pi$ (0) for Δ_1 (Δ_2), showing antiphase (in-phase) relation between Δ_1 (Δ_2) and the atomic topography.



Extended data Fig. 6 | Intra-unit-cell superconducting coherence peak sharpness modulation in another region (Region 2) of Sample 2. **a**, The topographic image of Region 2. **b,c**, D_1 (**b**) and D_2 (**c**) maps measured in the same area as in **a**, which show the intra-unit-cell modulations. The insets of **b** and **c** are the magnitude of the Fourier transform of **b** and **c**, respectively. The modulation wavevector peaks at the Bragg points of the topmost Te/Se lattice (Q_a and Q_b) are denoted by orange circles. **d,e**, The Fourier filtered gap map of D_1 (**d**) and D_2 (**e**). The topmost Te/Se sites within one unit cell are marked by black circles in **a-e**, clearly revealing the antiphase relation between $D_1(\mathbf{r})$ and $T(\mathbf{r})$ and in-phase relation between $D_2(\mathbf{r})$ and $T(\mathbf{r})$. **f**, The distributions of relative phase between superconducting coherence peak sharpness (D_1 in black or D_2 in red) and atomic topography. The relative phase distributions peak near $\pm\pi$ (0) for D_1 (D_2), showing antiphase (in-phase) relation between D_1 (D_2) and the atomic topography.



Extended data Fig. 7 | Intra-unit-cell superconducting gap modulation in Sample 1. **a**, The topographic image of the same area shown in Fig. 2. **b,c**, Superconducting gap maps of Δ_1 (**b**) and Δ_2 (**c**) measured in the same area as in **a**, which show the intra-unit-cell superconducting gap modulations. The insets of **b** and **c** are the magnitude of the Fourier transform of **b** and **c**, respectively. The modulation wavevector peaks at the Bragg points of the topmost Te/Se lattice (\mathbf{Q}_a and \mathbf{Q}_b) are denoted by orange circles. **d,e**, The Fourier filtered gap map of Δ_1 (**d**) and Δ_2 (**e**). The topmost Te/Se sites within one unit cell are marked by black circles in **a**, **d** and **e**, revealing the antiphase relation between $\Delta_{1,2}(\mathbf{r})$ and $T(\mathbf{r})$. **f**, The distributions of relative phase between superconducting gap size (Δ_1 in black or Δ_2 in red) and atomic topography. The relative phase distributions peak near $\pm\pi$, approximately showing the antiphase relation between the gap size and the atomic topography.



Extended data Fig. 8 | Intra-unit-cell superconducting coherence peak sharpness modulation in Sample 1. **a**, The topographic image of the same area shown in Fig. 2. **b,c**, D_1 (**b**) and D_2 (**c**) maps measured in the same area as in **a**, which show the intra-unit-cell modulations. The insets of **b** and **c** are the magnitude of the Fourier transform of **b** and **c**, respectively. The modulation wavevector peaks at the Bragg points of the topmost Te/Se lattice (Q_a and Q_b) are denoted by orange circles. **d,e**, The Fourier filtered gap map of D_1 (**d**) and D_2 (**e**). The topmost Te/Se sites within one unit cell are marked by black circles in **a-e**, clearly revealing the antiphase relation between $D_1(\mathbf{r})$ and $T(\mathbf{r})$ and in-phase relation between $D_2(\mathbf{r})$ and $T(\mathbf{r})$. **f**, The distributions of relative phase between superconducting coherence peak sharpness (D_1 in black or D_2 in red) and atomic topography. The relative phase distributions peak near $\pm\pi$ (0) for D_1 (D_2), showing antiphase (in-phase) relation between D_1 (D_2) and the atomic topography.